Rotational Symmetry Effects on Multibody Lateral Interactions between Co-Adsorbates at Heterogeneous Interfaces

Shuqiao Wang and Alyssa J.R. Hensley*

Cite This: *ACS Phys. Chem Au* 2024, 4, 328−335

Read Online

ACCESS | Metrics & More | Article Recommendations | Supporting Information

ABSTRACT: Heterogeneous interfaces are critical in a wide range of applications, and their material properties can be tuned via changes in the coverage and configuration of chemical adsorbates. However, the tunability of such adlayers is limited by a lack of knowledge surrounding the impact of adsorbate internal structure and rotational symmetry on lateral interactions between coadsorbates. Using density functional theory (DFT) and cluster expansions, we systematically determine the impacts of rotational symmetry on lateral interactions between coadsorbates as a function of DFT functional, adsorbate type, metal type, and cluster configuration. Results indicate that the rotational symmetry effects can be nearly exclusively partitioned into the shortest 2-body clusters. By electronic analysis, the nature and strength of such effects on the lateral interactions are attributed to a balance of repulsive and attractive electrostatic interactions that are dependent on the adsorbate and metal types. Taken together, our characterization of the impacts of adsorbate internal structure and rotational symmetry on lateral interactions enables improved accuracy within multiscale modeling of multibody adsorbates at heterogeneous interfaces.

KEYWORDS: *Heterogeneous interface, adsorption, multibody adsorbates, lateral interactions, rotational symmetry, density functional theory*
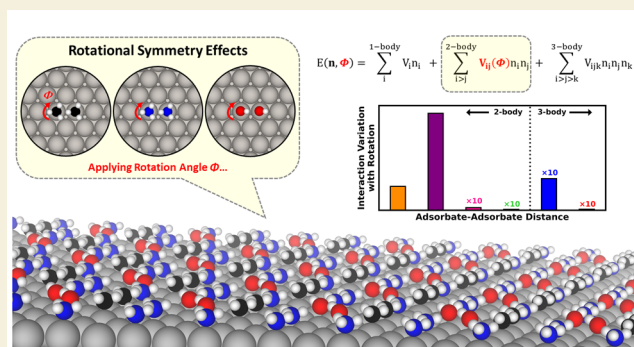
Heterogeneous interfaces—gas or liquid contacting a solid surface—are important for a wide range of applications, including catalysis,[1−3] semiconductors,[4,5] photochemistry,[6,7] and energy storage systems.[8,9] The material properties of such interfaces can be tuned via chemical adsorption.[10,11] However, precise control of surface material properties and chemical adsorption/desorption processes is complicated via nanoscale lateral interactions between coadsorbates,[12,13] which govern adsorbate coverage and configuration and ultimately the thermodynamic and kinetic behaviors of the interface.

Many theoretical approaches—including mean-field approximations, cluster expansions (CEs), force fields, and machine learning (ML)—have been applied to capture coverage and configuration effects for heterogeneous interfaces. The mean-field approximation is a simple, fast approach where each individual adsorbate is assumed to be affected by an averaged effect among all other adsorbates on the surface, regardless of configuration.[14,15] Despite extensive applications,[15−21] this method is limited when lateral interactions are strongly configuration-dependent. Meanwhile, CEs are direct quantifications of the total energy based on physically defined 1-, 2-, 3-, and higher-body "cluster" interactions between adsorbates.[22−24] The weight of each cluster's contribution to the total energy is determined by its effective cluster interaction (ECI),[25,26] which is parametrized based on the relative

distance between coadsorbates alone. Force fields, such as CHARMM, can be adapted to simulate the adsorbate−surface interactions, involving both intramolecular and intermolecular terms describing the internal structure, electrostatic interactions, van der Waals interactions, etc.[27−30] Notably, there is no explicit term within the CHARMM potential energy function that identifies key cluster configurations and quantifies the magnitude of the intermolecular rotational symmetry effects. Finally, various ML algorithms have become an appealing strategy to accelerate the study of coverage effects at heterogeneous interfaces over the years.[31−34]

Currently, configuration-dependent lateral interactions have been examined with CE and ML approaches for heterogeneous interfaces with small molecules, including H,[35,36] O,[37−41] CO,[42−44] and NO.[45,46] Notably, such simple adsorbates can be treated as symmetric point charges without internal chemical structure and no variation in lateral interaction strength based
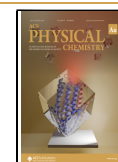
on relative orientation (i.e., rotational symmetry) between coadsorbates.[15,47] Outside of a CE applied to capture rotational symmetry effects in $H_2O/Pt(111)$,[48] the mean-field approximation is still the primary approach used to study coverage effects among large, internally complex molecules (e.g., aromatics,[15,20,21] carboxylic acids[49−51]).

Critically, quantification of the effect of internal chemical structure and rotational symmetry between coadsorbates on lateral interaction strength is missing, which can significantly impact predictions of dominant coverages and configurations for many-body adsorbates at heterogeneous interfaces.

Here, we present a systematic study quantifying the impacts of adsorbate internal structure and rotational symmetry on the lateral interactions calculated under the CE framework (Figure 1). Using density functional theory (DFT), we determine the
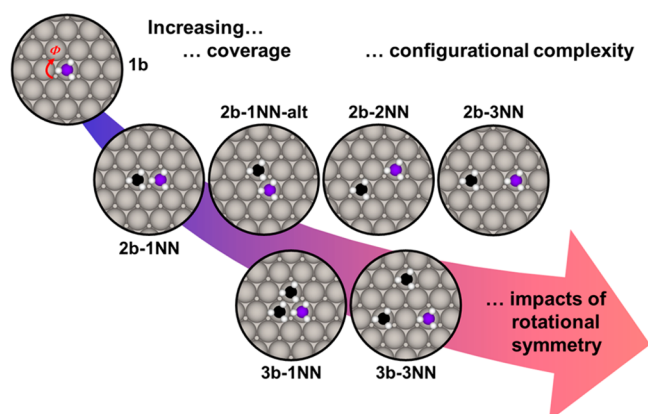

Figure 1. Increasing surface coverage of adsorbates impacts adlayer configurational complexity, including the often-neglected effects of rotational symmetry in adsorbates. We quantify rotational symmetry effects in adsorbate−adsorbate interactions by calculating the ECIs for a series of adsorbates on metal (111) facets as one adsorbate is rotated in-place by 60°. Shown are the top views for $CH_3/Pt(111)$. The silver, black, purple, and white spheres represent Pt, C (fixed), C (rotated), and H, respectively.

effect of rotational symmetry on the ECIs for a series of common 1-, 2-, and 3-body clusters based on DFT functional (i.e., RPBE, optB88-vdW), adsorbate type (i.e., CH_3, NH_3, OH), and metal type (i.e., Pt(111), Au(111)). Overall, our parametrization of rotational symmetry effects on lateral interactions sheds light on the origin of such effects as well as the importance of considering their contribution for large, internally complex adsorbates. These results advance our knowledge of under what conditions (e.g., DFT functional, intraspecies distance, cluster type, metal type, adsorbate type) rotational symmetry effects between coadsorbates are remarkable for the multiscale modeling (e.g., kinetic Monte Carlo) of complex heterogeneous interfaces.

The change in ECI strength during rotation of one adsorbate through relative angles of 0°−60° are fully illustrated here based on DFT functional (RPBE, optB88-vdW), adsorbate type (CH_3, NH_3, OH), metal type (Pt, Au), and configurational complexity which includes a series of 2- and 3-body interactions (Figure 1). Here, the ECIs for all adsorbates and configurations on Pt(111) and Au(111) are shown in Figure 2 and Figure S1, respectively. Furthermore, the variation in ECI strength with rotation angle was quantified as the root mean squared difference (RMSD) between the ECI at angle Φ

relative to 0° (Figure 2 and Figure S1 for Pt(111) and Au(111), respectively).

While the functional choice has been shown in previous work to significantly affect the magnitude of adsorption energies,[52−54] we find here that both the ECI values and overall trends for both functionals are nearly identical (Figure 2). For all adsorbates, metals, and configurations, the overall difference in the ECIs between the RPBE and optB88-vdW functionals was calculated as the RMSD (Table S3), which ranged from 0.0080 eV ($CH_3/Pt(111)$ in the 3b-3NN configuration) to 0.097 eV ($CH_3/Pt(111)$ in the 2b-1NN cluster). The largest differences in functional choice are seen in the 2b-1NN and 2b-1NN-alt clusters for all of the adsorbate cases (Table S3). In particular, the optB88-vdW functional lowers ECI strengths of the attractive 2b-1NN cluster in adsorbed OH due to hydrogen bonding; however, the net difference remains small (i.e., 0.082 eV for OH/Pt(111), 0.083 eV for OH/Au(111)). Overall, the choice of DFT functional results in relatively small changes to the ECI strengths and no changes in the ECI trends with configuration. Subsequent discussions here will focus on the RPBE functional results. Such uniform consistency among DFT functionals is powerful as model accuracy can be improved continuously by calculating the near-zero coverage adsorption energies (easily obtained) with higher accuracy functionals without having to repeat CE parametrizations (computationally intensive).

The interplay between rotational symmetry effects on ECI strengths and adsorbate−adsorbate distance is examined here to identify the minimum cluster size at which point the internal structure of adsorbates becomes important to the lateral interactions. By scanning through a series of 2- and 3-body clusters with various adsorbate−adsorbate distances, it is clear that the majority of rotational symmetry effects are isolated to the shortest 2-body interactions (i.e., 2b-1NN and 2b-1NN-alt). In the $CH_3/Pt(111)$ case (Figure 2A), both interactions have almost equivalent ECI strength (~0.86 eV) at 0°. As rotation angle increases, opposite behaviors in terms of ECI strengths occur for the two 2-body systems. The intensity for 2b-1NN-alt rapidly rises to the maximum of 2.71 eV, while 2b-1NN shows a lower ECI strength of 0.49 eV. This indicates that an increasing rotation angle strongly reinforces repulsive interactions in the 2b-1NN-alt cluster and gradually eases such interactions for the 2b-1NN cluster. Notably, the 3b-1NN interactions, which are related to a coexistence of 2b-1NN and 2b-1NN-alt interactions, are shown to have almost no dependence on rotational symmetry. Overall, the clusters' ECI behaviors with adsorbate−adsorbate distance shed light on the rotational symmetry effect, suggesting that even in tight triangular patterns, the rotational symmetry effects can be nearly exclusively partitioned into the 2b-1NN and 2b-1NN-alt interactions. Higher order 2-body interactions (i.e., 2b-2NN, 2b-3NN) show nearly no response to rotation angle, indicating the rotational symmetry effect has disappeared with increased adsorbate−adsorbate distance. These trends in ECI strength with cluster type and adsorbate−adsorbate distance hold true for all of the adsorbate and metal types tested here.

Examining the effect of adsorbate type on ECI strength leads to additional insights from the intrinsic adsorbate nature. Comparing ECI results between CH_3 and NH_3, both adsorbates have parallel trends in their ECI curves with rotation on both Pt(111) (Figure 2A,B) and Au(111) (Figure S1). The absolute ECI strengths of 2b-1NN and 2b-1NN-alt at 0° for NH_3 are stronger than CH_3, but the span of ECI
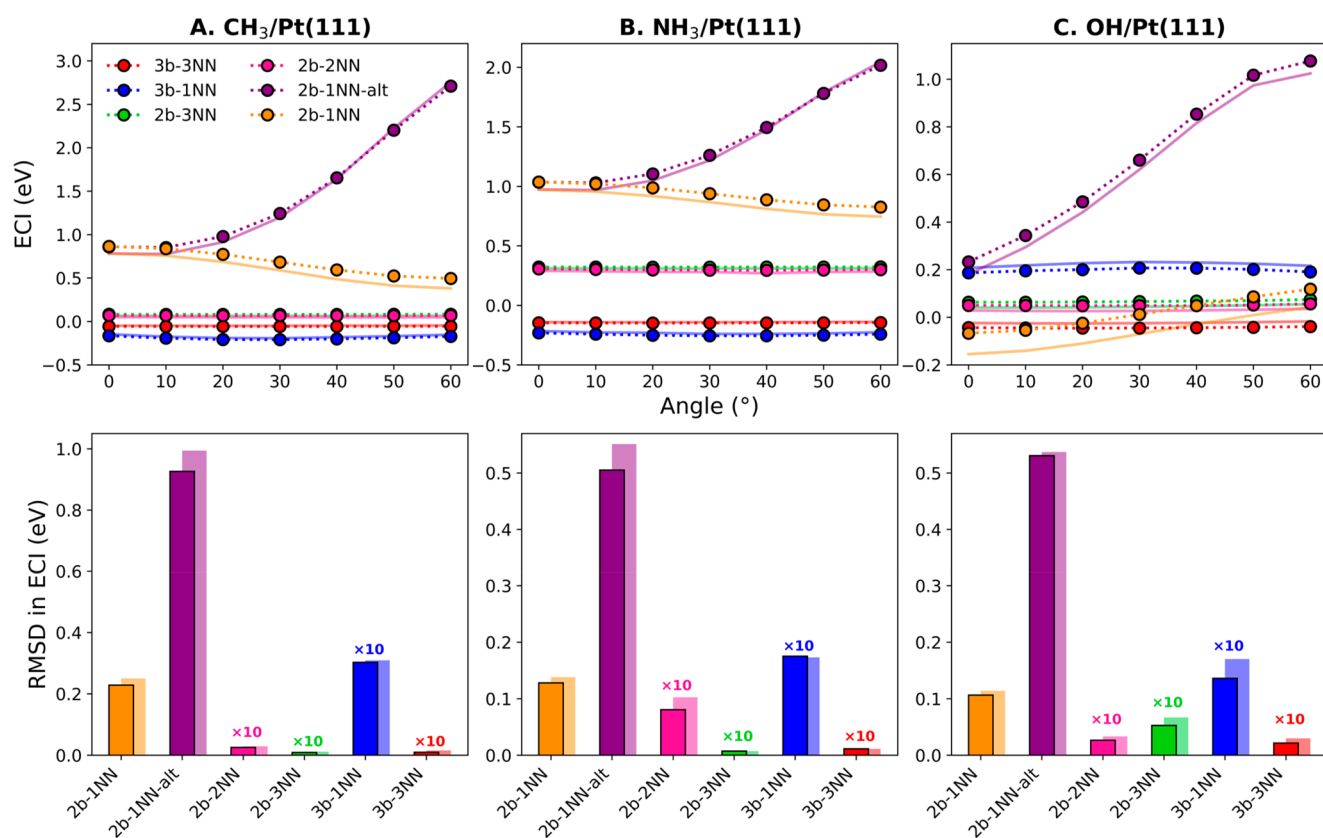
Figure 2. (Upper Panels) ECI strength for tested 2- and 3-body lateral interactions as a function of the rotation angle for one adsorbate (i.e., (A) CH$_3$, (B) NH$_3$, or (C) OH) relative to fixed neighbors on Pt(111). Results from two DFT functionals are shown: RPBE (circles and dotted lines) and optB88-vdW (transparent solid line). (Lower Panels) RMSDs induced in each tested ECI as a function of rotational angle for one adsorbate relative to fixed neighbors on Pt(111). Results from two DFT functionals shown: RPBE (solid) and optB88-vdW (transparent).

strength with rotation angle is smaller for NH$_3$ compared to CH$_3$ (i.e., 0.13/0.51 eV compared to 0.23/0.93 eV, respectively, for 2b-1NN/2b-1NN-alt on Pt(111), Figure 2A,B). Examining results for OH, the ECI strength for the 2b-1NN-alt cluster follows a trend similar to that of CH$_3$ and NH$_3$, incrementally increasing with increased rotation angle (span of ECI strength of 0.53 eV on Pt(111), Figure 2C). However, the 2b-1NN cluster for OH differs from the prior trend observed for CH$_3$ and NH$_3$, with the ECI strength for OH increasing with rotation from −0.07 to 0.12 eV on Pt(111) (Figure 2C). The energetic variations give a subsequent span of ECI strength of 0.11 eV. These trends in ECI strength with adsorbate type are consistent for all metal types tested here.

Just as how ECI strengths behave when adsorbate rotation is introduced in Pt(111) systems regarding various aspects discussed above, analogous trends are observed in Au(111) systems (Figure S1). Differently, the intensity of ECI variations is evidently reduced on Au(111). Taking 2b-1NN-alt as an example, the ECI strength at 0° for CH$_3$, NH$_3$, and OH on Au(111) is 0.58, 0.59, and 0.21 eV, respectively, while Pt(111) results have ECIs of 0.86, 1.04, and 0.23 eV. The corresponding ECI spans between 0° and 60° are 1.05, 0.56, and 0.48 eV on Au(111) and 1.85, 0.98, and 0.85 eV on Pt(111). Notably, such energetic differences between the two metals are directly related to the 1-body adsorption energies (Tables S1 & S2) and are a consequence of the two metals' electronic structure. The filled 5d subshell in Au contributes to the metal's stability, while Pt is more reactive due to unpaired

5d electrons.[55] These results are consistent with previously observed trends for coverage-dependent adsorptions on monometallic surfaces of Pt(111) and Au(111) from both mean-field[18] and CE approaches.[40]

To better understand the underlying chemical cause of rotational symmetry effects on adsorbate−adsorbate interactions, electronic investigations were conducted on the 2-body interaction cases where major ECI variations were observed during adsorbate rotation (2b-1NN, 2b-1NN-alt). First, examination of the d-band center in Pt(111) for both 2-body interactions with all three adsorbate types show negligible response during rotation (Table S5 and Figure S2). This suggests that adsorbate-induced changes in d-band centers present only a mean-field effect (e.g., dependent only on number of adsorbates and not configuration). Second, a Bader charge analysis applied to the 2-body clusters (Table S6) showed the charge variation on the adsorbate atom centers (e.g., H, C/N/O, or total adsorbate charge) during adsorbate rotation to be trivial. This indicates that adsorbates can accept or donate charge to the surface, but such behavior is almost independent of rotation/cluster type.

Taken together, the observed changes in the ECI strength for 2b-1NN and 2b-1NN-alt with rotation are not due to variations in either adsorbate−surface orbital rehybridization or permanent charge redistribution. What remains is a purely electrostatic effect resulting from a convolution of repulsive and attractive Coulombic potentials, according to
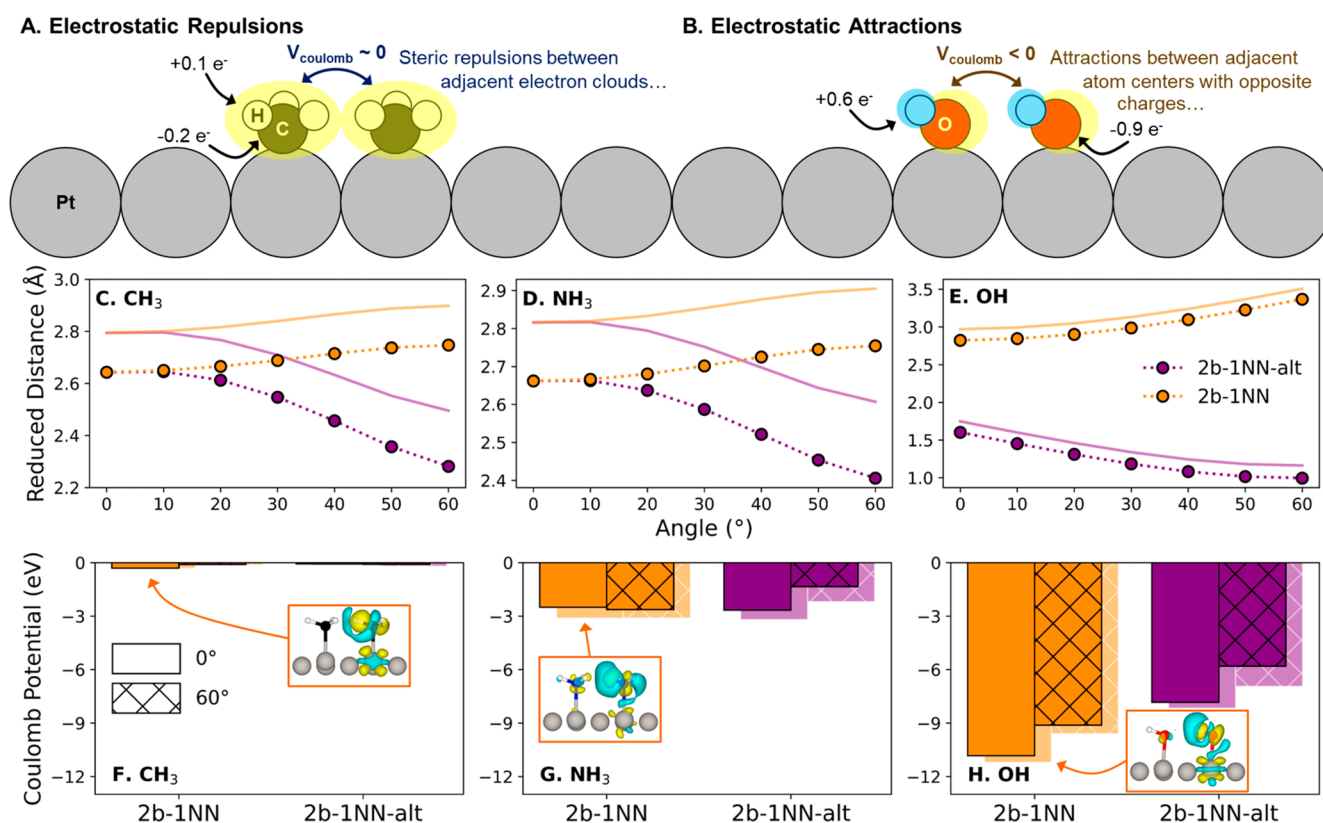
Figure 3. Schematic depiction of (A) repulsive and (B) attractive electrostatic interactions at play between coadsorbates. The yellow (blue) regions show areas of electron gain (loss). Bader charges are shown for each atom type within the adsorbates. Reduced distance (C−E), used here to characterize the strength of steric repulsions, and Coulomb potential (F−H), used here to characterize the strength of electrostatic attractions, are shown as a function of the rotation angle for one adsorbate relative to fixed neighbors for (C, F) CH_3, (D, G) NH_3, and (E, H) OH on Pt(111) (solid) and Au(111) (transparent). (Insets) Differential charge densities for the 2b-1NN clusters in the 0° rotation on Pt(111) upon addition of the rotating adsorbate's H nearest the fixed adsorbate. Isosurface level was set at 0.0045 $e^−$/Bohr^3.

$$V_{Coulomb} = \sum \frac{q_{ref} q_i}{4\pi\varepsilon_0 r_i} \tag{1}$$

where q_{ref} is the charge on the atom chosen as reference for calculating potential, q_i is the charge on the ith atom within the given cluster (excluding reference atom), ε_0 is the vacuum permittivity, and r_i is the distance between the reference atom and the ith atom within the given cluster. Figure 3 shows these factors conceptually. The repulsive interactions between coadsorbates result from steric effects arising when one adsorbate rotates and the corresponding distance between the two adsorbates alters. Nonpolar and more charge-neutral adsorbates such as CH_3 will see predominantly steric repulsions resulting from energy-raising charge interactions between adjacent electron clouds (Figure 3A). While all systems will experience such repulsive steric effects, attractive electrostatic interactions will become more prevalent in more polar adsorbates (i.e., NH_3, OH) due to energy-lowering charge interactions between the net positively charged H and net negatively charged N/O (Figure 3B). Thus, the resulting net ECI strength and its dependence on rotational symmetry will depend on the balance of repulsive and attractive electrostatic interactions. The dominance of the electrostatic effect on changes in ECI with adsorbate rotation is consistent with the rotational symmetry effects being partitioned into the shortest 2-body clusters (i.e., 2b-1NN and 2b-1NN-alt).

To probe the underlying chemical nature of the repulsive steric effects, we first examine the CH_3/Pt(111) dataset as a case study, considering that CH_3 is nonpolar with negligible attractive electrostatic interactions expected. Within the purely repulsive interaction regime, changes in ECI strength with rotation in the 2b-1NN and 2b-1NN-alt clusters can be rationalized based on the relative distances between atoms within the coadsorbates. While the coadsorbates' center of mass does not change with rotation for CH_3, the relative distance between any two atoms within the coadsorbates does change. Due to the structure of CH_3, any one distance between atoms within coadsorbates does not describe the steric repulsions between the electron clouds on each coadsorbate. Thus, we have derived a parameter here called reduced distance that describes the net change in distance between all atoms within the coadsorbates (r_i), calculated according to eq 2.

$$r_{red} = \left(\sum \frac{1}{r_i}\right)^{-1} \tag{2}$$

Figure 3C shows the reduced distance between coadsorbates in the 2b-1NN and 2b-1NN-alt clusters for CH_3/Pt(111) as a function of rotation. For the 2b-1NN cluster, as rotation increases from 0° to 60°, the reduced distance between the CH_3 increases from 2.64 to 2.75 Å. Meanwhile, the 2b-1NN-alt cluster sees a decrease in reduced distance from 2.64 to 2.28 Å over the same degree of rotation. These changes in reduced distance are linearly related to the changes in ECI strength (Figure S3), suggesting that the ECI strength due to steric

repulsions is directly and exclusively related to the relative distance between the two CH_3 adsorbates.

As for NH_3, it shares a similar structure with CH_3 in both molecule size and spatial configuration, leading to comparable steric effects on the surface. However, steric repulsions alone fail to answer the noticeable decrease in ECI spans due to rotational symmetry in the 2b-1NN and 2b-1NN-alt clusters between NH_3 and CH_3. An examination of the changes in reduced distance with rotation for NH_3/Pt(111) shows the distance between coadsorbed NH_3 goes from 2.66 to 2.75 Å in 2b-1NN and from 2.66 to 2.41 Å in 2b-1NN-alt (Figure 3D), which changes are nearly identical to CH_3. However, the ECI spans for the 2b-1NN and 2b-1NN-alt clusters for CH_3 are ~2 times larger than those for NH_3. Thus, the steric repulsions between coadsorbed NH_3 must be reduced due to attractive electrostatic interactions between oppositely charged atoms (e.g., NH_3/Pt(111) see the N atom take on a net -1.1 e$^-$ while each H atom takes on a net $+0.4$ e$^-$).

We characterized the strength of such attractive electrostatic interactions by calculating the Coulomb potential (eq 1) felt by the H atom on the rotated adsorbate nearest the fixed adsorbate. Bader charges were calculated at the 0° and 60° rotations, and all the metal surface atoms were excluded. Use of Bader charges represents a mean-field approximation to such Coulomb potentials as the Bader charges reduce the charge density to single values on each atom center. As shown in Figure 3F, the attractive electrostatic interactions between CH_3 coadsorbates in both 2b-1NN and 2b-1NN-alt are nearly negligible (i.e., -0.07 to -0.30 eV). This lack of attractive electrostatic interactions is shown visually in the differential charge density for CH_3 in the 2b-1NN cluster at a rotation of 0° in the Figure 3F inset. Upon addition of the rotated adsorbate's H nearest the fixed adsorbate (i.e., $\Delta\rho = \rho[2CH_3/Pt] - \rho[(CH_3 + CH_2)/Pt] - \rho[H]$), there is no response in the charge density on the fixed CH_3 adsorbate. Meanwhile, the attractive electrostatic interactions between NH_3 under the same conditions are at least an order of magnitude larger (i.e., -1.34 to -3.19 eV, Figure 3G). The effect of the increase in Coulomb potential for NH_3 relative to CH_3 is demonstrated in the differential charge density for NH_3 (i.e., $\Delta\rho = \rho[2NH_3/Pt] - \rho[(NH_3 + NH_2)/Pt] - \rho[H]$, Figure 3G inset) with a noticeable interaction between the charge on the N of the fixed adsorbate with the nearest H on the rotating adsorbate. Furthermore, the changes in Coulomb potential for NH_3 with rotation are consistent with changes in ECI strength. Thus, we see the modification of steric repulsions by attractive electrostatic interactions in more polar adsorbates (i.e., NH_3) as compared to nonpolar adsorbates (i.e., CH_3), which ultimately cause the ECI span from rotational symmetry to significantly decrease.

Results from OH further elucidate the simultaneous effect of repulsive and attractive electrostatic interactions due to the rotational symmetry within the 2b-1NN and 2b-1NN-alt clusters. In the 2b-1NN cluster, the coadsorbate configuration at 0° favors hydrogen bond formation, with subsequent rotation to 60° breaking said hydrogen bond. The 2b-1NN-alt cluster has a more repulsive ECI at 0° compared to 2b-1NN as the coadsorbate configuration is less favorable for hydrogen bonding, with subsequent rotation to 60° seeing strongly repulsive ECIs due to the formation of a linear O−H···H−O configuration. Examining the reduced distances (Figure 3E) for these OH configurations shows consistent behavior to CH_3 and NH_3 for the 2b-1NN-alt cluster—decreasing reduced

distance produces a sharp increase in ECI strength—while an inverse trend is observed for the 2b-1NN cluster due to hydrogen bond formation. Similar to NH_3, the deviations in rotational symmetry effects for OH that are expected from purely steric repulsions are captured in the Coulomb potential (Figure 3H). The significant decrease in ECI span for OH in both the 2b-1NN and 2b-1NN-alt clusters is consistent with the increase in attractive electrostatic interactions between coadsorbed, polar OH (e.g., Coulomb potentials are negative and at least two orders of magnitude larger than CH_3). The most attractive Coulomb potential between coadsorbed OH is seen in the 2b-1NN cluster at a rotation of 0° (i.e., -10.83 and -11.21 eV for Pt(111) and Au(111), respectively), which is when the full hydrogen bond is present. Rotation to 60° in the 2b-1NN cluster results in a ~15% decrease in the Coulomb potential, consistent with the loss of the hydrogen bond. Rotation in the 2b-1NN-alt cluster from 0° to 60° for OH also decreases the attractive electrostatic interactions. The trends in Coulomb potential determined here are consistent with chemical intuition regarding nonpolar (CH_3) versus polar (NH_3, OH) adsorbates, with the charge interactions graphically demonstrated via differential charge densities. Thus, we see the influence of highly polar and charge-separated adsorbates in reducing the impacts of steric repulsions on rotational symmetry in lateral interactions due to energy lowering of attractive electrostatic interactions.

In conclusion, we have characterized the impact of rotational symmetry on the strength and nature of lateral interactions between multibody adsorbates at heterogeneous interfaces. Our results showed that both the ECI values and overall trends for different DFT functionals (RPBE, optB88-vdW) are nearly identical among all configurations. The rotational symmetry effects can be nearly exclusively partitioned into the shortest 2-body cluster interactions (i.e., 2b-1NN, 2b-1NN-alt) and are dependent on both adsorbate type, related to the polarity of adsorbates, and metal type, related to the metal's electronic structure and consequential 1-body adsorption energy. An electronic analysis of the 2-body clusters showed that changes in ECI strength due to rotational symmetry results from a convolution of repulsive and attractive Coulombic potentials, both of which change based on adsorbate type. Our work captures to what degree and under what conditions rotational symmetry coupling with internal adsorbate structure causes variations in lateral interactions. Such characterizations will enable improved accuracy within multiscale models of large, internally complex multibody adsorbates at heterogeneous interfaces.

■ COMPUTATIONAL METHODS

DFT calculations were performed using the Vienna *Ab Initio* Simulation Package (VASP).[56,57] The projector augmented wave (PAW) method[58,59] and a basis set of plane waves with a kinetic energy cutoff of 400 eV were applied. Both the revised Perdew−Burke−Ernzerhof (RPBE)[60] and optB88-vdW[61,62] functionals were employed to describe the electron exchange and correlation. The tolerances for the ionic and electronic relaxations were 2×10^{-2} eV/Å and 1×10^{-4} eV, respectively. The Methfessel Paxton[63] ($N = 1$) smearing method was used with a smearing width of 0.1 eV.

The Pt(111) and Au(111) slabs were modeled with a p(4 × 4) supercell with four atomic layers. The top two layers were allowed to relax during optimization, while the bottom two layers were held fixed at their bulk positions. The first Brillouin zone was sampled using a gamma centered **k**-point grid of (4 × 4 × 1) for slab calculations. Due to periodic boundary conditions, repeating slabs were separated by a

vacuum spacing of at least ~14.6 Å to eliminate interactions in the $\hat{z}$-direction. Optimum lattice constants for Pt and Au calculated with the RPBE/optB88-vdW functional were 3.990/3.979 and 4.199/4.162 Å, respectively, with a gamma centered **k**-point grid of (20 × 20 × 20). Calculations for reference molecules in the gas phase were performed using a (14 × 15 × 16) Å box with one single **k**-point, the gamma point. All ground state conformations (i.e., ionic relaxation) were determined using the conjugate gradient method.

The effect of rotational symmetry on the lateral interaction strength was tested using three distinct surface adsorbates (i.e., CH_3, NH_3, OH), varying different properties in bond polarity, chemical structure, and adsorption energy. The tested adsorbate configurations at 1/16, 2/16, and 3/16 monolayers (ML, 1 ML = 1 adsorbate/1 surface atom) on both Pt(111) and Au(111) are shown in Figure 1. At the near zero coverage used here (i.e., 1/16 ML), ground state optimizations were performed for each possible adsorption site (i.e., top, bridge, fcc, and hcp) for all adsorbate/metal/functional combinations (Tables S1 & S2). The top site was found to be the most energetically favorable for all combinations, except for OH, which prefers the bridge site on Pt(111) by ≤0.1 eV and the fcc site on Au(111) by ≤0.3 eV. To ensure comparability between results from all adsorbate/metal/functional combinations tested here, we placed all adsorbates at the top site.

Upon finding the dominant adsorption sites for all adsorbate/metal/functional combinations, we performed a series of single point calculations for a range of configurations (Figure 1). For each configuration, one adsorbate was rotated by 60° in increments of 10° while the other adsorbates were fixed. The 60° maximum rotation was sufficient to capture the 6-fold, hexagonal symmetry of the (111) facet. At each rotation, the total adsorption energy was calculated according to

$$E_{ads} = E[N_{ads}X/M(111)] - E[M(111)] - N_{ads}E[X] \qquad (3)$$

where $E[N_{ads}X/M\,(111)]$, $E[M\,(111)]$, and $E[X]$ are the total energies of the adsorbate-covered (111) surface, clean (111) surface (M = Pt or Au), and gas-phase species (X = CH_3, NH_3, or OH), respectively, while N_{ads} is the number of adsorbates. The total adsorption energy, $E_{ads}(\mathbf{n})$, can be decomposed into a series of configuration-dependent terms (i.e., clusters) with associated weights (i.e., effective cluster interactions, ECIs) via the lattice gas (LG) CE method,[22,25,36] according to

$$E_{ads}(\mathbf{n}) = \sum_{i}^{1\text{-body}} V_i n_i + \sum_{i>j}^{2\text{-body}} V_{ij} n_i n_j + \sum_{i>j>k}^{3\text{-body}} V_{ijk} n_i n_j n_k + \ldots \qquad (4)$$

where the system's geometric configuration is denoted as $\mathbf{n} = \{n_1, n_2, \cdots, n_i, \cdots\}$, a vector of occupation variables, where each n_i takes on a value of either 0 or 1, determined by the vacancy or occupancy of the ith lattice site, respectively. The terms V_i, V_{ij}, V_{ijk}, and so forth represent the 1-, 2-, and 3-body ECIs, and so on, individually. As ECI strength is known to decay with increasing distance between coadsorbates,[37–39,41–43] we focus here on six of the shortest 2- and 3-body interactions (Figure 1). The complete dataset of adsorption energies and calculated ECIs are given for all adsorbate/metal/functional combinations in the Supporting Information.

ASSOCIATED CONTENT

Supporting Information

The Supporting Information is available free of charge at https://pubs.acs.org/doi/10.1021/acsphyschemau.4c00019.

Adsorption site testing at low coverage (i.e., 1/16 ML); effect of rotational symmetry on ECI strength and RMSD for all adsorbates on Au(111); quantification of DFT functional effect on ECI strength due to rotational symmetry; electronic properties (i.e., d-band center, Bader charge) for select cluster configurations as a function of rotational symmetry; linear relation between ECI strength and reduced distance for select cluster configurations; top views of all tested cluster configurations; complete dataset of adsorption energies and ECI strengths for all combinations as a function of rotational symmetry (PDF)

AUTHOR INFORMATION

Corresponding Author

Alyssa J.R. Hensley − *Department of Chemical Engineering and Materials Science, Stevens Institute of Technology, Hoboken, New Jersey 07030, United States;* orcid.org/0000-0002-7382-1286; Email: ahensley@stevens.edu

Author

Shuqiao Wang − *Department of Chemical Engineering and Materials Science, Stevens Institute of Technology, Hoboken, New Jersey 07030, United States;* orcid.org/0000-0003-2470-9447

Complete contact information is available at:
https://pubs.acs.org/10.1021/acsphyschemau.4c00019

Author Contributions

CRediT: **Shuqiao Wang** data curation, formal analysis, investigation, methodology, visualization, writing-original draft, writing-review & editing; **Alyssa J. R. Hensley** conceptualization, data curation, formal analysis, funding acquisition, investigation, methodology, project administration, resources, software, supervision, visualization, writing-original draft, writing-review & editing.

Notes

The authors declare no competing financial interest.

REFERENCES

(1) Gao, W.; et al. Interfaces in Heterogeneous Catalysts: Advancing Mechanistic Understanding through Atomic-Scale Measurements. *Acc. Chem. Res.* **2017**, *50*, 787−795.

(2) Zhang, Z.; et al. Ensembles of Metastable States Govern Heterogeneous Catalysis on Dynamic Interfaces *Acc. Chem. Res.* **2020**, *53*, 447−458.

(3) Zhao, Q.; Xu, Y.; Greeley, J.; Savoie, B. M.; et al. Deep Reaction Network Exploration at a Heterogeneous Catalytic Interface. *Nat. Commun.* **2022**, *13*, 4860.

(4) Thoss, M.; et al. Theoretical Study of Ultrafast Heterogeneous Electron Transfer Reactions at Dye−Semiconductor Interfaces. *Chem. Phys.* **2004**, *304*, 169−181.

(5) Nieto-Pescador, J.; et al. Photoinduced Ultrafast Heterogeneous Electron Transfer at Molecule−Semiconductor Interfaces. *J. Phys. Chem. Lett.* **2014**, *5*, 3498−3507.

(6) Matsumoto, Y. Toward Photochemistry of Integrated Heterogeneous Systems. *J. Chem. Phys.* **2012**, *137*, No. 091705.

(7) George, C.; et al. Heterogeneous Photochemistry in the Atmosphere. *Chem. Rev.* **2015**, *115*, 4218−4258.

(8) Wang, S.; et al. Heterogeneous Interface-Derived Engineered Electronic Structure of SiO with Enhanced Lithium Storage. *ACS Appl. Energy Mater.* **2022**, *5*, 750−759.

(9) Xiao, B.; et al. 2D Dynamic Heterogeneous Interface Coupling Endowing Extra Zn^{2+} Storage. *Adv. Funct. Mater.* **2023**, *33*, No. 2211679.

(10) Xu, W. P.; Xu, H. Role of Surface Adsorption in Tuning the Properties of Black Phosphorus. *Phys. Chem. Chem. Phys.* **2018**, *20*, 112−117.

(11) Gil, A. Classical and New Insights into the Methodology for Characterizing Adsorbents and Metal Catalysts by Chemical Adsorption. *Catal. Today* **2023**, *423*, No. 114016.

(12) Matera, S.; et al. Progress in Accurate Chemical Kinetic Modeling, Simulations, and Parameter Estimation for Heterogeneous Catalysis. *ACS Catal.* **2019**, *9*, 6624−6647.

(13) Li, X.; Grabow, L. C. Evaluating the Benefits of Kinetic Monte Carlo and Microkinetic Modeling for Catalyst Design Studies in the Presence of Lateral Interactions. *Catal. Today* **2022**, *387*, 150−158.

(14) Sillar, K.; et al. Ab Initio Adsorption Isotherms for Molecules with Lateral Interactions: CO_2 in Metal−Organic Frameworks. *J. Phys. Chem. C* **2017**, *121*, 12789−12799.

(15) Chaudhary, N.; et al. Coverage-Dependent Adsorption of Phenol on Pt(111) from First Principles. *J. Phys. Chem. C* **2020**, *124*, 356−362.

(16) Grabow, L. C.; et al. Understanding Trends in Catalytic Activity: The Effect of Adsorbate−Adsorbate Interactions for CO Oxidation Over Transition Metals. *Top. Catal.* **2010**, *53*, 298−310.

(17) Lausche, A. C.; et al. On the Effect of Coverage-Dependent Adsorbate−Adsorbate Interactions for CO Methanation on Transition Metal Surfaces. *J. Catal.* **2013**, *307*, 275−282.

(18) Miller, S. D.; et al. Configurational Correlations in the Coverage Dependent Adsorption Energies of Oxygen Atoms on Late Transition Metal FCC(111) Surfaces. *J. Chem. Phys.* **2011**, *134*, No. 104709.

(19) Wang, S.; Hensley, A. J. R. Probing the Nanoscale Driving Forces for Adsorbate-Induced $Rh_{50}Pd_{50}$ Nanoparticle Reconstruction via Mean-Field Models of Multi-Faceted Nanoparticles. *Catal. Sci. Technol.* **2024**, *14*, 1122−1137.

(20) Wong, B. M.; et al. Benchmarking the Accuracy of Coverage-Dependent Models: Adsorption and Desorption of Benzene on Pt (1 1 1) and Pt_3Sn (1 1 1) from First Principles. *Prog. Surf. Sci.* **2019**, *94*, No. 100538.

(21) Cardwell, N.; et al. Capturing the Coverage Dependence of Aromatics' Adsorption through Mean-Field Models. *J. Phys. Chem. A* **2023**, *127*, 10693−10700.

(22) Sanchez, J. M.; et al. Generalized Cluster Description of Multicomponent Systems. *Phys. A: Stat. Mech. Appl.* **1984**, *128*, 334−350.

(23) Sanchez, J. M. Cluster Expansions and the Configurational Energy of Alloys. *Phys. Rev. B: Condens. Matter Mater. Phys.* **1993**, *48*, 14013−14015.

(24) Sanchez, J. M. Cluster Expansion and the Configurational Theory of Alloys. *Phys. Rev. B: Condens. Matter Mater. Phys.* **2010**, *81*, No. 224202.

(25) Collinge, G.; et al. Formulation of Multicomponent Lattice Gas Model Cluster Expansions Parameterized on Ab Initio Data: An Introduction to the Ab Initio Mean-Field Augmented Lattice Gas Modeling Code. *J. Phys. Chem. C* **2020**, *124*, 2923−2938.

(26) Collinge, G.; et al. Quantifying Errors in Effective Cluster Interactions of Lattice Gas Cluster Expansions. *J. Phys. Chem. C* **2022**, *126*, 1289−1302.

(27) Mackerell, A. D., Jr Empirical Force Fields for Biological Macromolecules: Overview and Issues. *J. Comput. Chem.* **2004**, *25*, 1584−1604.

(28) Brooks, B. R.; et al. CHARMM: The Biomolecular Simulation Program. *J. Comput. Chem.* **2009**, *30*, 1545−1614.

(29) Vanommeslaeghe, K.; et al. CHARMM General Force Field: A Force Field for Drug-Like Molecules Compatible with the CHARMM All-Atom Additive Biological Fforce Fields. *J. Comput. Chem.* **2010**, *31*, 671−690.

(30) Bramley, G. A.; et al. The Application of QM/MM Simulations in Heterogeneous Catalysis. *Phys. Chem. Chem. Phys.* **2023**, *25*, 6562−6585.

(31) Behler, J.; Parrinello, M. Generalized Neural-Network Representation of High-Dimensional Potential-Energy Surfaces. *Phys. Rev. Lett.* **2007**, *98*, No. 146401.

(32) Kitchin, J. R. Machine Learning in Catalysis. *Nat. Catal.* **2018**, *1*, 230−232.

(33) Mou, T.; et al. Machine Learning of Lateral Adsorbate Interactions in Surface Reaction Kinetics. *Curr. Opin. Chem. Eng.* **2022**, *36*, No. 100825.

(34) Ghanekar, P. G.; et al. Adsorbate Chemical Environment-Based Machine Learning Framework for Heterogeneous Catalysis. *Nat. Commun.* **2022**, *13*, 5788.

(35) Binder, K.; Landau, D. P. Square Lattice Gases with Two- and Three-Body Interactions: A Model for the Adsorption of Hydrogen on Pd(100). *Surf. Sci.* **1981**, *108*, 503−525.

(36) Hensley, A. J. R.; et al. Coverage-Dependent Adsorption of Hydrogen on Fe(100): Determining Catalytically Relevant Surface Structures via Lattice Gas Models. *J. Phys. Chem. C* **2020**, *124*, 7254−7266.

(37) Stampfl, C.; et al. First-Principles Theory of Surface Thermodynamics and Kinetics. *Phys. Rev. Lett.* **1999**, *83*, 2993−2996.

(38) McEwen, J.-S.; et al. Phase Diagram of O/Ru(0001) from First Principles. *Chem. Phys. Lett.* **2002**, *361*, 317−320.

(39) Schmidt, D. J.; et al. Performance of Cluster Expansions of Coverage-Dependent Adsorption of Atomic Oxygen on Pt(111). *J. Chem. Theory Comput.* **2012**, *8*, 264−273.

(40) Frey, K.; et al. Implications of Coverage-Dependent O Adsorption for Catalytic NO Oxidation on the Late Transition Metals. *Catal. Sci. Technol.* **2014**, *4*, 4356−4365.

(41) Bray, J.; et al. Predicting the Electric Field Effect on the Lateral Interactions Between Adsorbates: O/Fe(100) from First Principles. *Top. Catal.* **2018**, *61*, 763−775.

(42) McEwen, J.-S.; et al. Adsorption and Desorption of CO on Pt(111): A Comprehensive Analysis. *Surf. Sci.* **2003**, *545*, 47−69.

(43) Payne, S. H.; et al. Adsorption and Desorption of CO on Ru(0001): A Comprehensive Analysis. *Surf. Sci.* **2005**, *594*, 240−262.

(44) Klumpers, B.; et al. Lateral Interactions of Dynamic Adlayer Structures from Artificial Neural Networks. *J. Phys. Chem. C* **2022**, *126*, 5529−5540.

(45) Lym, J.; et al. Lattice Convolutional Neural Network Modeling of Adsorbate Coverage Effects. *J. Phys. Chem. C* **2019**, *123*, 18951−18959.

(46) Bajpai, A.; et al. Comparison of Coverage-Dependent Binding Energy Models for Mean-Field Microkinetic Rate Predictions. *Langmuir* **2020**, *36*, 465−474.

(47) Kose, R.; et al. Role of Lateral Interactions in Adsorption Kinetics: CO/Rh{100}. *J. Phys. Chem. B* **1999**, *103*, 8722−8725.

(48) Karlberg, G. S.; Wahnström, G. Density-Functional Based Modeling of the Intermediate in the Water Production Reaction on Pt(111). *Phys. Rev. Lett.* **2004**, *92*, No. 136103.

(49) Lu, J.; et al. Theoretical Investigation of the Decarboxylation and Decarbonylation Mechanism of Propanoic Acid over a Ru(0001) Model Surface. *J. Catal.* **2015**, *324*, 14−24.

(50) Mamun, O.; et al. Theoretical Investigation of the Hydrodeoxygenation of Levulinic Acid to γ-Valerolactone over Ru(0001). *ACS Catal.* **2017**, *7*, 215−228.

(51) Yang, W.; et al. Unraveling the Mechanism of the Hydrodeoxygenation of Propionic Acid over a Pt (1 1 1) Surface in Vapor and Liquid Phases. *J. Catal.* **2020**, *381*, 547−560.

(52) Wellendorff, J.; et al. Density Functionals for Surface Science: Exchange-Correlation Model Development with Bayesian Error Estimation. *Phys. Rev. B: Condens. Matter Mater. Phys.* **2012**, *85*, No. 235149.

(53) Wellendorff, J.; et al. A Benchmark Database for Adsorption Bond Energies to Transition Metal Surfaces and Comparison to Selected DFT Functionals. *Surf. Sci.* **2015**, *640*, 36−44.

(54) Hensley, A. J. R.; et al. DFT-Based Method for More Accurate Adsorption Energies: An Adaptive Sum of Energies from RPBE and vdW Density Functionals. *J. Phys. Chem. C* **2017**, *121*, 4937−4945.

(55) Wang, H.; et al. Effect of Reducible Oxide−Metal Cluster Charge Transfer on the Structure and Reactivity of Adsorbed Au and Pt Atoms and Clusters on Anatase TiO_2. *J. Chem. Phys.* **2017**, *146*, No. 184703.

(56) Kresse, G.; Hafner, J. Ab Initio Molecular Dynamics for Liquid Metals. *Phys. Rev. B: Condens. Matter Mater. Phys.* **1993**, *47*, 558−561.

(57) Kresse, G.; Furthmüller, J. Efficient Iterative Schemes for Ab Initio Total-Energy Calculations Using a Plane-Wave Basis Set. *Phys. Rev. B: Condens. Matter Mater. Phys.* **1996**, *54*, 11169−11186.

(58) Blöchl, P. E. Projector Augmented-Wave Method. *Phys. Rev. B: Condens. Matter Mater. Phys.* **1994**, *50*, 17953−17979.

(59) Kresse, G.; Joubert, D. From Ultrasoft Pseudopotentials to the Projector Augmented-Wave Method. *Phys. Rev. B: Condens. Matter Mater. Phys.* **1999**, *59*, 1758−1775.

(60) Hammer, B.; et al. Improved Adsorption Energetics within Density-Functional Theory Using Revised Perdew-Burke-Ernzerhof Functionals. *Phys. Rev. B: Condens. Matter Mater. Phys.* **1999**, *59*, 7413−7421.

(61) Klimeš, J.; et al. Chemical Accuracy for the van der Waals Density Functional. *J. Phys.: Condens. Matter* **2010**, *22*, No. 022201.

(62) Klimeš, J.; et al. Van der Waals Density Functionals Applied to Solids. *Phys. Rev. B: Condens. Matter Mater. Phys.* **2011**, *83*, No. 195131.

(63) Methfessel, M.; Paxton, A. T. High-Precision Sampling for Brillouin-Zone Integration in Metals. *Phys. Rev. B: Condens. Matter Mater. Phys.* **1989**, *40*, 3616−3621.